Noname manuscript No.
(will be inserted by the editor)

Fast Parameter Calibration of a Cardiac Electromechanical Model from Medical Images based on the Unscented Transform

Stéphanie Marchesseau · Hervé Delingette · Maxime Sermesant · Nicholas Ayache

Accepted for publication in Sept 2012

Abstract Patient-specific cardiac modelling can help in understanding pathophysiology and predict therapy planning. However it requires to personalize the model geometry, kinematics, electrophysiology and mechanics. Calibration aims at providing proper initial values of parameters before performing the personalization stage which involves solving an inverse problem. We propose a fast automatic calibration method of the mechanical parameters of a complete electromechanical model of the heart based on a sensitivity analysis and the Unscented Transform algorithm. A new implementation of the complete Bestel-Clement-Sorine (BCS) cardiac model is also proposed, in a modular and efficient framework. A complete sensitivity analysis is performed that reveals which observations on the volume evolution are significant to characterize the global behaviour of the myocardium. We show that the calibration method gives satisfying results by optimizing up to 5 parameters of the BCS model in only one iteration. This method was evaluated synthetically as well as on 7 volunteers with a mean relative error from the real data of 10%. This calibration is designed to replace manual parameter estimation as well as initialization steps that precede automatic personalization algorithms based on images.

Keywords Computer Model · Cardiac Mechanics · Parameter Calibration · Medical Images · Unscented Transform

Stéphanie Marchesseau
INRIA, Asclepios Research Project, Sophia Antipolis, France
Tel.: +334-92-387151
E-mail: Stephanie.Marchesseau@inria.fr

Hervé Delingette · Maxime Sermesant · Nicholas Ayache
INRIA, Asclepios Research Project, Sophia Antipolis, France

1 Introduction

The clinical understanding and treatment of cardiovascular diseases is highly complex and includes a wide range of therapies: from drug therapy to Radiofrequency Ablation (RFA) aiming at reducing Ventricular Tachycardia (VT) or Atrial Fibrillation (AF), also including Cardiac Resynchronization Therapy (CRT) aiming at relieving Heart Failure (HF) symptoms with the implantation of pacemaker leads (Smith et al, 2011). Optimizing the leads configuration, selecting suitable patients, estimating regions to be ablated are difficulties that face the cardiologists for each patient. In order to provide additional guidance to cardiologists, many research groups are investigating the possibility to plan such therapies based on biophysical models of the heart (Kerckhoffs, 2010). The hypothesis is that one may combine anatomical and functional data to build patient-specific cardiac models that could have the potential to predict the benefit of the therapies. Cardiac electromechanical simulations are based on computational models that can represent the heart geometry, motion and electrophysiology patterns during a cardiac cycle with sufficient accuracy. Integration of anatomical, mechanical and electrophysiological information for a given subject is essential to build such models.

Several approaches for the past 20 years have been developed to describe and simulate cardiac function, including cardiac mechanics and electrophysiology (Humphrey et al, 1990; Hunter et al, 1997; Nash, 1998; Bestel et al, 2001; Sachse, 2004). They differ in their choice of hyperelastic material, electrophysiological properties or electromechanical coupling. In this paper the Bestel-Clement-Sorine (BCS) model (Bestel et al, 2001), further improved by (Chapelle et al, 2012),

is used for its consistency with thermodynamical requirements in its continuous as well as in its discrete form (Sainte-Marie et al, 2006). Moreover it has demonstrated a good predictive power under different pacing conditions in terms of haemodynamics (Sermesant et al, 2012).

The simulation becomes patient-specific after several levels of personalization: geometrical (a computational mesh is built from patient-specific anatomical images (see Fig. 1), kinematic (the motion of the cardiac structure is estimated from cine-MR images (McLeod et al, 2012; Sermesant et al, 2006)), electrophysiological (the depolarization and repolarization times are extracted from electrocardiograms (Relan et al, 2011)) and mechanical. The focus of this paper is on the latter personalization level, which consists in optimizing mechanical parameters of the model so that the simulation behaves in accordance to patient-specific datasets (images and other signals).

This inverse problem has been tackled by different authors. For instance, (Xi et al, 2011) and (Liu and Shi, 2009) estimate the passive material stiffness with data assimilation methods while (Wang et al, 2009) use Sequential Quadratic Programming. (Moireau and Chapelle, 2011) as well as (Chabiniok et al, 2011) estimate the contractility parameters using Reduced Unscented Kalman Filtering. (Sundar et al, 2009) and (Delingette et al, 2011) rather use adjoint data assimilation methods.

All these methods are time consuming since they require an important number of simulations. Moreover, there is no guarantee that such algorithms converge toward a relevant solution due to their dependence on initial range of parameter values since it is often necessary to be close to the solution for the algorithm to converge toward the global minimum. The choice of the parameters to estimate and their initial calibration have therefore great impact for the personalization.

Our main contribution tackles this initialization issue: we propose a simple and efficient method to automatically calibrate the parameters from the ventricular volume evolution over the cardiac cycle. It has been applied successfully for the calibration of mechanical parameters from 7 healthy cases. Our proposed method is based on the Unscented Transform algorithm and requires only one iteration with multiple simulations performed in parallel for calibrating typically 4 or 5 parameters selected from a sensitivity analysis.

Our approach remains tractable (computational time around 20 minutes for a tetrahedral mesh of 80,000 elements) due to a novel and efficient implementation of the BCS model in the interactive framework SOFA[1]. It also includes the changes of cardiac phases through a valve model and takes into account the mechanical effect of the pericardial sac.

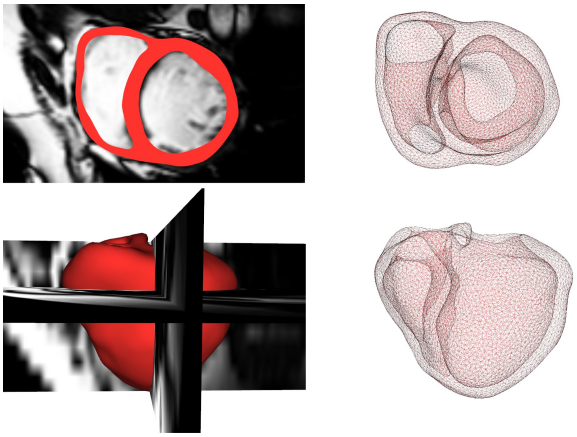

Fig. 1: Extracted myocardium meshes including the two ventricles and the four valves, segmented from 3D MRI.

2 Materials and Methods

2.1 Data Acquisition

We demonstrate the application of the proposed method on cardiac MRI data, including both SSFP sequence for anatomical description and cine-MRI for motion tracking. Data were acquired at the Division of Imaging Sciences & Biomedical Engineering at King's College London, UK, as part of studies that were ethically approved.

2.1.1 Volunteer Study

This study includes an extensive multi-modality imaging of volunteers from which seven healthy cases were used. All datasets consist of sequences of 4D cine-MRI with a spatial resolution of approximately $1.5\times1.5\times7\text{mm}^3$ and a temporal resolution of around 30 ms (30 images per cardiac cycle), that cover the ventricles entirely. Volunteers were aged 28 ± 5 years, and supposed to be without clinical history of cardiac diseases. This dataset was made available to the research community for the STACOM'2011 challenge, see (Tobon-Gomez et al, 2011) for details regarding the data acquisition of this study.

[1] SOFA is an Open Source medical simulation software available at www.sofa-framework.org

2.1.2 Clinical Data Pre-Processing

Three different steps are needed before any mechanical personalization can be performed: extraction of the myocardium geometry, estimation of the patient's cardiac motion and personalization of the electrophysiological propagation.

Geometry Personalization

To personalize the geometry from images, we used Philips automatic cardiac segmentation (Ecabert et al, 2011) in GIMIAS[2] to extract the ventricles from the SSFP sequence and then recreate a binary mask of the myocardium. We then used CGAL[3] meshing software to create tetrahedral meshes. In the electromechanical model presented in Section 2.2, fibre directions play an important role for both electrophysiological and mechanical simulations. There are several ways to generate realistic fibre directions: by mapping an atlas onto the myocardium geometry (Peyrat et al, 2007; Lombaert et al, 2011; Toussaint et al, 2010) or by synthetically using prescribed values of helix angles across the myocardium wall. In this paper, the fibres were created synthetically with angles varying linearly from -70° to +70° across the myocardial wall (from epicardium to endocardium).

Kinematics personalization

A non-rigid registration algorithm was applied to the clinical 4D image sequences to find the deformation field between the end diastolic image and each subsequent image. We used the incompressible Log-Domain Demons (iLogDemons) developed by (Mansi et al, 2011) which estimates a dense non linear transformation that best aligns a template image to a reference image. Moreover, it allows to recover some components of the twist motion of the myocardium by incorporating an elastic and an incompressible regularizer into the registration.

Electrophysiology personalization

To simulate the electrophysiological pattern of activity, an Eikonal model was solved for the depolarization time T_d at each point of the mesh: $v\sqrt{\nabla T_d^t \mathbf{D} \nabla T_d} = 1$. v is the local electrical conduction velocity and $\mathbf{D} = (1-r)\mathbf{f} \otimes \mathbf{f} + r\mathbf{I}$ is the anisotropic conductivity tensor which depends on the fibre orientation $\mathbf{f}$ and on an anisotropic ratio r. The solution of this electrophysiological model was performed using multi-front Fast Marching Method which also computes the repolarization times (Sermesant et al, 2007) taking into account a restitution curve. For patient data, the personalization of this model requires to specify the onset of the electrical propagation (corresponding to the extremities of the Purkinje network) and the conduction velocity. No subject specific electrophysiological data were acquired and therefore standard values were assumed (conduction velocity of 900mm/s). The simulation of electrophysiology leads to the estimation of depolarization and repolarization times that then serve as inputs for the mechanical contraction.

[2] GIMIAS is a workflow-oriented environment focused on biomedical image computing and simulation (Larrabide et al, 2009)

[3] CGAL is a Computational Geometry Algorithms Library. It is available at http://www.cgal.org

2.2 Electromechanical Modelling of the Heart: The Bestel-Clement-Sorine Model

We describe in this section, the modelling and numerical methods used to represent the mechanical behaviour of the heart. Our approach is based on the Bestel-Clement-Sorine (BCS) model (Bestel et al, 2001) further improved by (Chapelle et al, 2012). This choice is governed by some good properties of the BCS model: It is based on a multi-scale analysis, is compatible with the laws of thermodynamics (balance of energy may be written), takes into account *the Starling effect*. Moreover, the model has been shown to represent rather well (Chabiniok, 2011) the physiological behavior of a myocardial fibre based on a quantitative comparison with a rodent papillary muscle under isotonic, isometric contractions measured experimentally.

The model is composed of a passive isotropic visco-hyperelastic component that accounts for the elasticity and the friction in the cardiac extracellular matrix (mainly collagen and elastic) surrounding the fibres. In parallel, the stress along the cardiac fibre is composed of an active part (contraction in the sarcomere) and a passive part corresponding to the elastic bound (titin) between sarcomeres and Z-discs. The contractile component, driven by the control variable u, has a viscous part to account for the energy dissipated in the sarcomere due to friction. The elasticity of the titin is the component that allows the isometric behaviour of the cardiac fibre. Fig. 2 shows a rheological representation of this model.

The equations are summarized here to introduce its parameters and to describe its implementation based on the SOFA platform.

2.2.1 Passive Non-Linear Elasticity

In the BCS approach, the extracellular matrix is considered to be a passive hyperelastic material. Several authors (Holzapfel and Ogden, 2009; Wong et al,

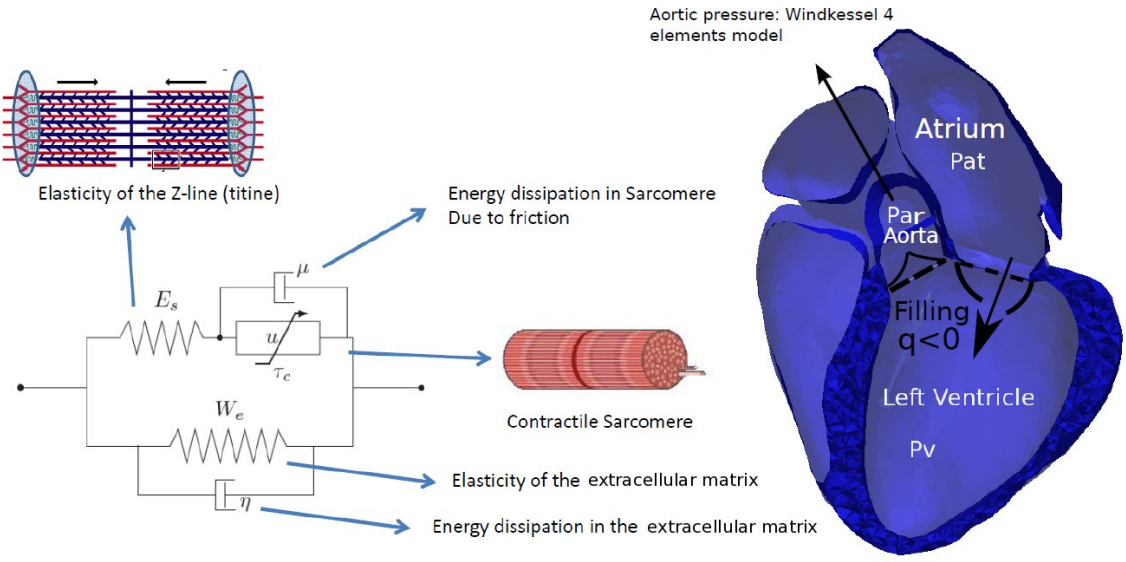

Fig. 2: Full electromechanical and circulation model. (Left) W_e is the strain energy of the extracellular matrix considered here as an isotropic material, associated with a dissipative term η. u is a control variable which is driven by changes in transmembrane potential. It controls the contraction stress τ_c. μ deals with the friction in the sarcomere while E_s is a linear spring to enforce elasticity of the titin. (Right) Circulation model in the filling phase for the left ventricle.

2008; Mazhari and McCulloch, 2000) consider the myocardium as a whole to have an orthotropic behavior (such as the Costa's law (Costa et al, 2001)), taking into account both fibre and laminar sheets directions. In this paper, we consider an isotropic behavior described as a Mooney Rivlin material. Thus globally, adding the elasticity of the Z-discs, the passive behavior of myocardial tissue in the BCS model is considered to be transversally isotropic. An exponential hyperelastic material has been considered in (Chabiniok, 2011) instead of Mooney-Rivlin but with limited benefits due to its contraction behavior. Orthotropic materials may be introduced in the future by integrating recent work from Lombaert et al (2011) which estimates the laminar sheets direction on human hearts.

Linear tetrahedral finite elements are used to discretize the strain energy describing the Mooney-Rivlin material. Instead of the classical Bubnov-Galerkin Finite Element Method (FEM) formulation, the energy is discretized with the MJED (Multiplicative Jacobian Energy Decomposition) technique described in (Marchesseau et al, 2010). This method is equivalent to the classical FEM but allows to quickly assemble the stiffness matrix of any hyperelastic materials by precomputing some of its terms. The strain energy for Mooney Rivlin material is given as:

$$W_e = c_1(\bar{I}_1 - 3) + c_2(\bar{I}_2 - 3) + \frac{K}{2}(J-1)^2 \qquad (1)$$

where c_1, c_2 are material parameters and K is the Bulk modulus. The quantities $\bar{I}_1$ and $\bar{I}_2$ are the isochoric invariants of the *Cauchy-deformation tensor* $\mathbf{C} = \nabla\phi^T\nabla\phi$: $\bar{I}_1 = J^{-2/3}I_1$, $\bar{I}_2 = J^{-4/3}I_2$ where $I_1 = tr\mathbf{C}$, $I_2 = \frac{1}{2}((tr\mathbf{C})^2 - tr\mathbf{C}^2)$ and J is the Jacobian $J = det\nabla\phi$.

2.2.2 Active Fibre Contraction

The active component is added to account for the contraction of the sarcomere. The contraction stress tensor σ_c is in parallel with a viscosity element (cf Fig. 2) which gives $\sigma_c = \tau_c + \mu\dot{e_c}$. A linear elastic component having stress $\sigma_s = E_s e_s$ is in series with the contractile component. Therefore, after linearization of the equations presented by (Chapelle et al, 2012), $e_{1D} = e_s + e_c$ and $\sigma_c = \sigma_s$, where e_{1D} is the projection of the Green-Lagrange deformation tensor $\mathbf{E}$ on the fibre direction: $e_{1D} = \mathbf{f}^T\mathbf{E}\mathbf{f}$. At the nanoscopic scale, the binding and unbinding process of the actin and myosin filaments in the sarcomere is described by Huxley filament model (Huxley, 1957). Statistical mechanics allows to describe its behavior at the macroscopic scale, resulting in a differential equation that controls the active stress τ_c and the sarcomere stiffness k_c:

$$\begin{cases} \dot{k_c} = -(\mid u \mid + \alpha \mid \dot{e_c} \mid)k_c + n_0 k_0 \mid u \mid_+ \\ \dot{\tau_c} = -(\mid u \mid + \alpha \mid \dot{e_c} \mid)\tau_c + \dot{e_c}k_c + n_0\sigma_0 \mid u \mid_+ \end{cases} \qquad (2)$$

where α is a constant related to the cross-bridge release due to a high contraction rate, k_0 and σ_0 are respectively the maximum stiffness and contraction. n_0 is a reduction factor that allows to take into account *the Starling effect* by which the maximum contraction

depends on the fibre strain e_c. The control variable u is derived from the electrical activation model and is a function of the free calcium concentration only. It can be summarized as:

$$\begin{cases} u(t) = k_{ATP} & \text{when } T_d \leq t \leq T_d + APD \\ u(t) = -k_{RS} & \text{when } t < T_d \text{ and } t > T_d + APD \end{cases} \tag{3}$$

k_{ATP} is the rate of the myosin ATPase activity controlling the contraction rate and k_{RS} is the rate of sarcoplasmic reticulum calcium re-uptake controlling the relaxation rate. T_d and APD are respectively the depolarization time and the action potential duration (time during which the cell stays excited). These two values are obtained by a biophysical model of cardiac electrophysiology. Finally, the density of strain energy to add to the passive model is $W_c = \sigma_c \mathbf{f}^T \mathbf{E}\mathbf{f}$.

Our implementation in SOFA first solves the coupled differential equations (2) with an Euler implicit solver, and then computes the required force fields and stiffness matrices for the global system. Appendix A provides additional details about the discretized equations.

2.2.3 Haemodynamic Model

The ventricles are filled with blood coming from the atria and ejected through the arteries. A basic circulation model is represented in Fig. 2 and represents the four phases of the cardiac cycle, independently for each ventricle as follows:

- *Filling*: while the ventricular pressure (P_v) is below the atrium pressure (P_{at}), the mitral (or tricuspid) valve is open and the ventricle fills up with blood.
- *Isovolumetric Contraction*: the contraction starts and all valves are closed.
- *Ejection*: when $P_v > P_{ar}$ the arterial pressure, the aortic (or pulmonary) valve opens and the blood is ejected from the ventricle.
- *Isovolumetric Relaxation*: the relaxation starts and all valves are closed.

To model those phases we apply the haemodynamic model introduced by (Chapelle et al, 2012). It gives a relation between the blood flow leaving the ventricle (q) and the atrial, ventricular and aortic pressures:

$$q = \begin{cases} K_{at}(P_v - P_{at}) & \text{for } P_v \leq P_{at} \\ K_{iso}(P_v - P_{at}) & \text{for } P_{at} < P_v \leq P_{ar} \\ K_{ar}(P_v - P_{ar}) + K_{iso}(P_{ar} - P_{at}) & \text{for } P_v > P_{ar} \end{cases} \tag{4}$$

where K_{at} and K_{ar} correspond to linear laws and K_{iso} relaxes the usual isovolumetric constraint ($q = 0$). With this definition, K_{iso} is much smaller than K_{at} and K_{ar}. The aortic pressure is computed following the fourth-element Windkessel model described in Appendix B. Windkessel model depends on four parameters: the peripheral resistance R_p, the characteristic time τ, the characteristic resistance Z_c and the total arteria inertance L. The initial and asymptotic arterial pressures also influence the model. The atrial pressure is computed analytically as two sigmoids and depends on an initial and a maximum pressure that is set from the literature (Schäffler and Schmidt, 1999). The sigmoids start during the relaxation and finish before the beginning of the next contraction. An adjustment is set *a posteriori* to fit the volume or pressure curves.

To apply this model we need to solve the following dynamical system, simultaneously for both ventricles, with the pressure vector $\mathbf{P_v} = [P_{vL}, P_{vR}]$:

$$\begin{bmatrix} \mathbf{K} & \mathbf{G}^T \\ \mathbf{G} & \mathbf{D} \end{bmatrix} \begin{bmatrix} \Delta\mathbf{s} \\ \mathbf{P_v} \end{bmatrix} = \begin{bmatrix} \mathbf{F} \\ \mathbf{F}_D \end{bmatrix}$$

where $\mathbf{K}\Delta\mathbf{s} = \mathbf{F}$ is the unconstrained dynamical system including passive and active elasticities, and $\mathbf{s}$ the unknown nodal velocities. $\mathbf{G} = [\mathbf{G}_L, \mathbf{G}_R]$ is the derivative of the volume with respect to the positions: $\mathbf{G}^T\Delta\mathbf{u} = \Delta\mathbf{V}$ where $\mathbf{u}$ are the unknown positions of the points and $\mathbf{V} = [V_L, V_R]$ is the volume of the ventricles (see Appendix B). $\mathbf{F}_D = [F_{DL}, F_{DR}]$ and $\mathbf{D} = [D_L, D_R]$ are set for each phase to verify:

$$\mathbf{G}\Delta\mathbf{s} + \mathbf{D}\mathbf{P_v} = \mathbf{F_D} \tag{5}$$

(see B for a detailed derivation of this equation from eq(4)). To solve the dynamical system $\mathbf{K}\Delta\mathbf{s}^{t+\Delta t} = \mathbf{F} - \mathbf{G}^T{\mathbf{P_v}}^{t+\Delta t}$ without adding state variables for $\mathbf{P_v}$, we design a prediction-correction algorithm to solve the constraint (Algorithm.1).

Algorithm 1 HaemodynamicModel() function

1: Solve $\mathbf{K}\Delta\tilde{\mathbf{s}}^{t+\Delta t} = \mathbf{F} - \mathbf{G}^T{\mathbf{P_v}}^t$
2: Using (5) and $\Delta\mathbf{s}^{t+\Delta t} = \Delta\tilde{\mathbf{s}}^{t+\Delta t} - \mathbf{K}^{-1}\mathbf{G}^T({\mathbf{P_v}}^{t+\Delta t} - P_v^t)$, rewrite $\mathbf{G}\Delta\tilde{\mathbf{s}}^{t+\Delta t} - \mathbf{B}({\mathbf{P_v}}^{t+\Delta t} - {\mathbf{P_v}}^t) = \mathbf{F}_D - \mathbf{D}{\mathbf{P_v}}^{t+\Delta t}$ with $\mathbf{B} = \mathbf{G}\mathbf{K}^{-1}\mathbf{G}^T$
3: Solve separately for each ventricle the equation $\mathbf{K}\mathbf{A} = \mathbf{G}^T$ with $\mathbf{A} = [\mathbf{A}_L, \mathbf{A}_R]$ to get $\mathbf{B} = \mathbf{G}\mathbf{A}$.
4: Compute the unknown pressure

$${\mathbf{P_v}}^{t+\Delta t} = (\mathbf{D} - \mathbf{B})^{-1}\left(\mathbf{F}_D - \mathbf{B}{\mathbf{P_v}}^t - \mathbf{G}\Delta\tilde{\mathbf{s}}^{t+\Delta t}\right)$$

5: Correct the velocity such as

$$\Delta\mathbf{s}^{t+\Delta t} = \Delta\tilde{\mathbf{s}}^{t+\Delta t} - \mathbf{A}({\mathbf{P_v}}^{t+\Delta t} - {\mathbf{P_v}}^t)$$

2.2.4 Boundary Conditions

Two types of boundary conditions were defined to prevent rigid body motion. First, the heart mesh is attached at the level of the four valve annuli limiting the ventricles. To allow some valve motion, linear springs connect the valve vertices to their reference position. We defined a unique stiffness matrix $\mathbf{K} = k_b\mathbf{Id}$ where k_b is the isotropic stiffness. Therefore the force for each node is defined as $F_i = \mathbf{K}(Q_i - P_i)$ where P_i is the initial position and Q_i is the current position. A value of $50\,Pa$ was chosen for the stiffness k_b so as to allow a small movement of the valves. This constraint has a noticeable impact on the motion of the myocardium, but not as much on the global indices of the volume and pressure. Second, we defined a fixed pericardium surface surrounding the myocardium which limits the ventricle displacements: each time a epicardium vertex hits the pericardial surface, a force is applied preventing the penetration. The pericardial surface was defined as an offset surface of the epicardium situated at a fixed distance ($\sim 2mm$) from the epicardium at end-diastolic time point and efficient collision detection was implemented in SOFA. This collision constraint enables to limit the radial body motion but does not impact the global volume or pressure evolution.

2.2.5 Implementation issues

The implementation of the BCS model in the SOFA platform differs from the one of (Chapelle et al, 2012) in several ways. In our approach, the fibre stresses and stiffness at each node are not added as state variables but are solved separately from the position and velocity variables with a weaker coupling. This allows us to have a better conditioned system of equations that is solved efficiently with regular linear solver such as pre-conditioned conjugated gradient. Furthermore, we have linearized the strain relation $e_{1D} = e_s + e_c$ in the active components and solved the valve model with a prediction-correction approach which requires 2 additional solutions of the linear system of equations per time step. Also, fast assembly of the stiffness matrix associated with passive hyperelastic material was reached with the MJED method. Finally, we added a pericardial constraint to limit the displacement of epicardium vertices. Efficient and interactive simulations were made possible thanks to the adoption of the simulation platform SOFA.

2.3 Sensitivity Analysis of Global Outputs to the Model Parameters

We propose in this paper a calibration method of the model parameters. A first step is to select the main parameters that can be estimated given the available data. To this end, we study the influence of each active, passive and heamodynamic model parameter on the volume, the outward flow ($q = -dV/dt$) and the pressure in the ventricle. This required about 160 simulations. The results are given in Section 3.3 only for the left ventricle since the right ventricle has a similar behaviour. The sensitivity analysis is performed with null initial velocities for two reasons: first, the cycle starts with the isovolumetric contraction phase so the initial velocity is small and second, the temporal samplings of the MRI datasets are too sparse (only 30 images for 0.93s) to precisely estimate the initial velocity. The results are shown for one volunteer geometry, similar results were found on different geometries. The variation of the parameters was chosen after a trial and error approach in order to obtain a physiologically realistic behaviour. The used minimum and maximum values are presented in Table 1.

Table 1: Ranges of parameter values explored in the sensitivity analysis.

Notation	Parameter Name	Min - Max
σ_0 (MPa)	Max Contraction	$4-10$
k_0 (MPa)	Max Stiffness	$3-9$
k_{ATP} (s^{-1})	Contraction Rate	$5-20$
k_{RS} (s^{-1})	Relaxation Rate	$5-60$
E_s (MPa)	Linear Modulus	$3-15$
α	Cross-bridges Unfasten Rate	$0-0.8$
μ (MPa.s)	Viscosity	$0.07-0.6$
c_1 (kPa)	Mooney Rivlin Modulus	$7-20$
c_2 (kPa)	Mooney Rivlin Modulus	$7-20$
K (MPa)	Bulk Modulus	$6-25$
τ (s)	Wind. Charact. Time	$0.4-2$
R_p (MPa.m^{-3}.s)	Wind. Periph. Resistance	$30-300$
Z_c (MPa.m^{-3}.s)	Wind. Charact. Resistance	$1-10$
L (kPa.s^2.m^{-3})	Wind. Total Art. Inertance	$1-100$

2.4 Parameters Calibration Based on Unscented Transform

From this qualitative study of the main model parameters, we determine a strategy to automatically assess the model parameters from the volume and flow curves. Since our goal is to calibrate and not to personalize the model, the method has to be fast and require minimal implementation. We chose the ventricular volume curves as main observation to perform the

calibration as they are important physiological indices and can be captured by few quantities: the minimum volume V_{min} (which could also be the ejection fraction since the maximum volume is constant over all cases), the maximum and minimum of the flow (q_{max} and q_{min} respectively).

2.4.1 Unscented Transform Algorithm

To calibrate the model, we use the algorithm derived from the Unscented Transform (Julier and Uhlmann, 1997). The proposed algorithm finds a set of parameters that minimizes the difference between the measured observation $\mathbf{Z}^{obs}$ and the predicted observation $\bar{\mathbf{Z}}$. It is explained as follows: Let $\mathbf{Z}$ be the vector of observations, here $\mathbf{Z} = [V_{min}, q_{max}, q_{min}]$ and $\mathbf{X}$ the parameter vector which has mean $\mathbf{X}^0$, covariance $\mathbf{C}_X$ and dimension n. We set the covariance as $\mathbf{C}_X = \mathbf{Cov}(\mathbf{X}, \mathbf{X})$ by estimating the minimal and the maximal value of each parameter with a trial and error approach. We compute observations $\mathbf{Z}_{i\varepsilon}$ from the $2n+1$ sets of parameters $\mathbf{X}_{i\varepsilon} = [x_1, x_2, ..., x_i + \varepsilon s_i, ...]$ around the mean value $\mathbf{X}^0$ where $\varepsilon \in \{-1, 0, 1\}$ and s_i is an uncertainty function of the covariance $s_i = \gamma\sqrt{\mathbf{C}_{Xi}}$, with γ the scaling parameters. The mean observation is set as $\bar{\mathbf{Z}} = \sum_{i,\varepsilon} \omega_{i\varepsilon} \mathbf{Z}_{i\varepsilon}$ with some weights $\omega_{i\varepsilon}$ described by (Wan and Van Der Merwe, 2000). Finally we derive the covariance matrix as:

$$\mathbf{Cov}(\mathbf{X}, \mathbf{Z}) = \sum_{i\varepsilon} \omega_{i\varepsilon} (\mathbf{X}_{i\varepsilon} - \mathbf{X}^0) \, (\mathbf{Z}_{i\varepsilon} - \bar{\mathbf{Z}})^T \tag{6}$$

The new set of parameters $\mathbf{X}^{new}$ found to match the observations $\mathbf{Z}^{obs}$ is

$$(\mathbf{X}^{new} - \mathbf{X}^0) = \mathbf{Cov}(\mathbf{X}, \mathbf{Z}) \, \mathbf{Cov}(\mathbf{Z}, \mathbf{Z})^{-1} \, (\mathbf{Z}^{obs} - \bar{\mathbf{Z}}) \tag{7}$$

where

$$\mathbf{Cov}(\mathbf{Z}, \mathbf{Z}) = \sum_{i\varepsilon} \omega_{i\varepsilon} (\mathbf{Z}_{i\varepsilon} - \bar{\mathbf{Z}}) \, (\mathbf{Z}_{i\varepsilon} - \bar{\mathbf{Z}})^T. \tag{8}$$

This algorithm is very simple to implement and runs in one iteration to give $\mathbf{X}^{new}$. Another simulation is necessary to obtain the resulting observation $\mathbf{Z}^{new}$.

2.4.2 Qualitative and Quantitative Parameter Selection

Sixteen parameters in total may be estimated: $(\sigma_0, k_{rs}, k_{atp}, k_0, \alpha, \mu, E_s)$ active parameters, (K, c_1, c_2) passive parameters and $(R_p, \tau, Z_c, L, K_{isoC}, K_{isoR})$ for the valve model. Since it is not reasonable to try to estimate all of them at once, we decide to set some of them to a standard value and estimate the remaining ones. The selection was made from the sensitivity analysis results and confirmed by a Singular Value Decomposition (SVD) of the covariance matrix $\mathbf{Cov}(\mathbf{X}, \mathbf{Z})$ between all 16 parameters and the three observations cited above $[V_{min}, q_{max}, q_{min}]$. Then, for each vector $\mathbf{X}_{i\varepsilon}$, the observations $\mathbf{Z}_{i\varepsilon}$ are computed (which corresponds to 33 simulations). The Singular Value Decomposition leads to $\mathbf{Cov}(\mathbf{X}, \mathbf{Z}) = \mathbf{USV}^T$ where $\mathbf{U}$ is a 16×16 unitary matrix whose columns are called the left singular vectors and represent the eigenvectors of $\mathbf{Cov}(\mathbf{X}, \mathbf{Z})\mathbf{Cov}(\mathbf{X}, \mathbf{Z})^T$. Four parameters were therefore selected (see Sec.3.2.4).

2.4.3 Computational Considerations

Before running the proposed algorithm, a few manual steps were performed on one volunteer case. First, γ and the weights $\omega_{i\varepsilon}$ have to be adjusted. They both depend on the dimension n and on a parameter α which represents the spread of the sigma points around $\mathbf{X}^0$ and is set to 10^{-1} (Wan and Van Der Merwe, 2000). Then, the covariance matrix $\mathbf{C}_X$ and the initial value $\mathbf{X}^0$ had to be defined and computed from a trial and error approach. Once calibrated on one volunteer, the same values were used on all the cases. To obtain the four parameters from this algorithm, nine independent simulations are required. To check the results, another simulation is performed and the resulting observations are compared to the data. When dealing with real data, a time shift is estimated *a posteriori* since the simulation does not start exactly at the same time and phase of the cycle as the time series of images. This time shift is computed in order to minimize the mean square difference between the volumes over time in the data (V^{obs}) and the ones after estimation of the parameters (V^{new}). Although the considered observations are time-invariant, we record this time shift since personalization techniques based on images require the simulation to be synchronized with the measurements. Finally, in order to fit the end-diastolic volume or pressure, the atrial pressure is manually adjusted.

3 Results

3.1 Forward Simulation of the Bestel-Clement-Sorine Model

The simulations were performed on a laptop PC with a Intel Core Duo processor at 2.80Hz and took about 10 minutes per cardiac cycle for meshes with about 80,000 tetrahedra. The time steps were set depending on the cardiac cycles and the number of images (for instance $dt = 7.75ms$ for 30 images and a heart period of 0.93s). A sensitivity study on the mesh quality and the

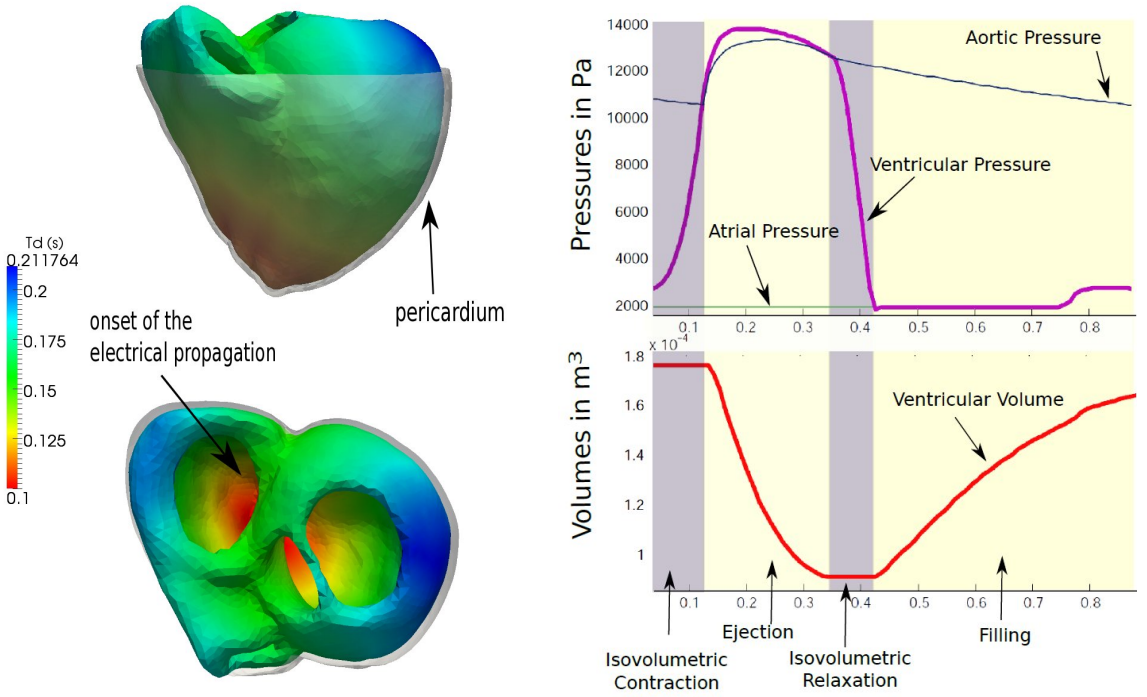

Fig. 3: (Left) Mesh and electrophysiological isochrones. (Right) Pressures and volumes curves resulting from the simulation of one cardiac cycle, for the left ventricle.

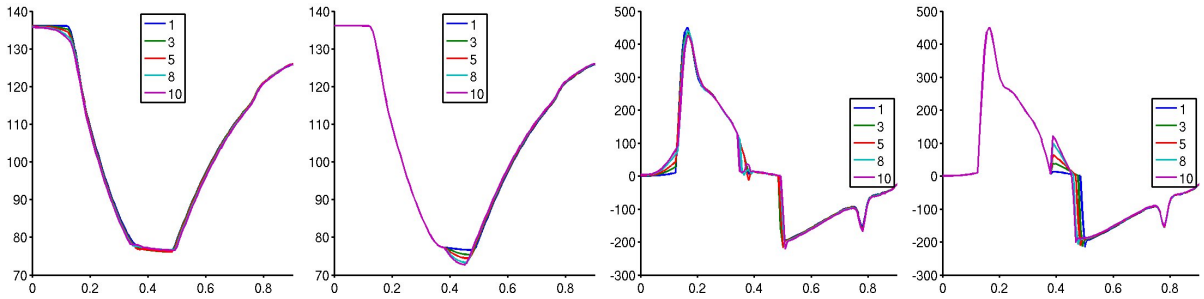

(a) Volume: K_{isoC} (b) Volume: K_{isoR} (c) Flow: K_{isoC} (d) Flow: K_{isoR}

Fig. 4: Volume (in mL) and outward flow (in $mL.s^{-1}$) evolution over time (in s) for the left ventricle, with varying isovolumetric factors. The local minimum of the flow at the end of the cycle represents the beginning of the atrial contraction.

time step showed that the chosen values lead to a good trade-off between computation time and accuracy. An example of resulting curves for the pressure and the volume in the left ventricle is given in Fig. 3 including the four cardiac phases. The duration of the isovolumetric phases depends on the factors K_{iso_C} and K_{iso_R} as shown on Fig. 4. The mesh and the electrophysiological mapping used for this simulation are also presented in Fig. 3. With this example, the power developed by the heart can be computed as $P = \Delta V_L \ \Delta P_{vL} \approx 1.3W$ which is in the range of $[1W, 2W]$ usually referenced in the literature.

3.2 Sensitivity Analysis of Global Outputs to the Model Parameters

Results of the sensitivity analysis on the volume, pressure and flow curves are presented below. For all the cases, the initial states of simulations are obtained with a mesh created from the segmentation of the end-diastole frame.

3.2.1 Active parameters

The active parameters mainly influence the volume curves in terms of amplitude, slopes or duration of the phases. Some of them also influence the pressure

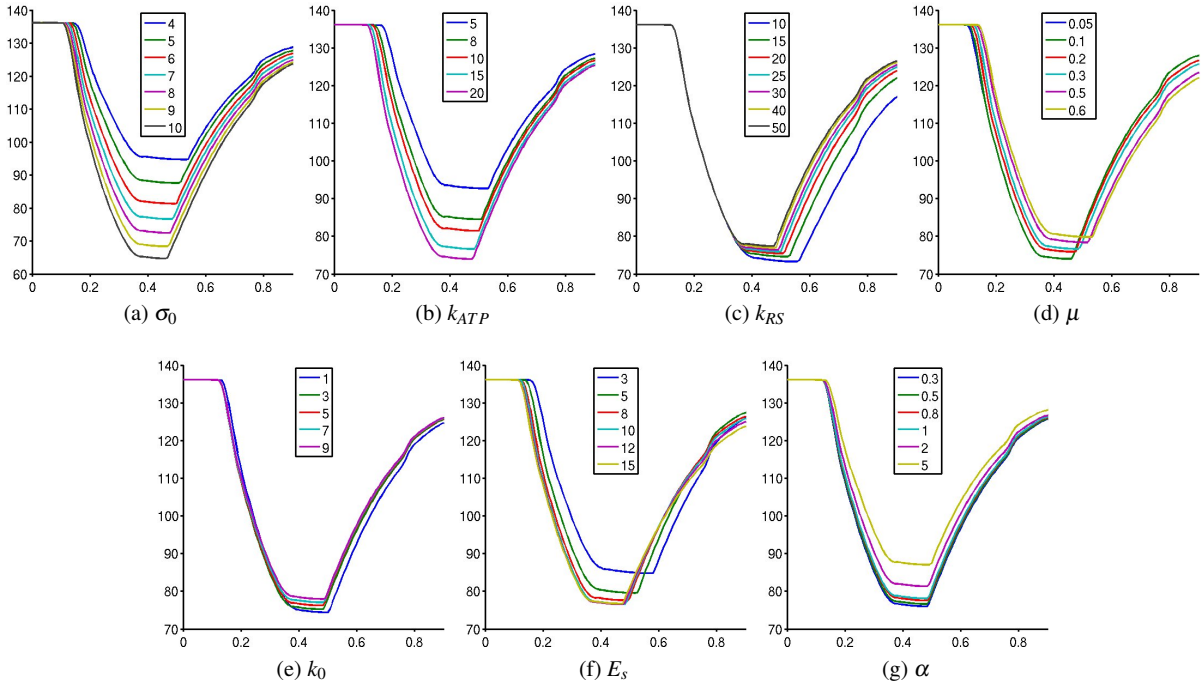

Fig. 5: Volume evolution (in *mL*) over time (in *s*) for the left ventricle, with varying active parameters.

curves. Relevant curves are presented in Fig. 5 for the volume and Fig. 6 for the pressure.

From these curves, we can conclude that the maximum contraction σ_0 and the contraction rate k_{atp} act together to increase the ejection fraction and change both the relaxation and the contraction slopes while the relaxation rate k_{rs} only influences the relaxation phase. The linear modulus E_s and the viscosity parameter μ modify the slopes and enable a complete cycle. Finally both the maximum stiffness k_0 and the cross-bridges unfasten rate α have a small influence on the ejection fraction. Similar conclusions can be drawn for the pressure curves: when a parameter acts on the ejection fraction it also acts on the maximum pressure, the pressure slopes are dependent on the same parameters as the volume slopes.

3.2.2 Passive Parameters

No significant differences in terms of pressure or volumes curves can be noticed between the two Mooney-Rivlin parameters c_1 and c_2, therefore the influence of only one of them is given in Fig. 7. Mooney Rivlin first modulus c_1 influences the ejection fraction and the maximum of pressure. The bulk modulus K greatly acts on the relaxation phase. Moreover, when those parameters are too large, the end-diastolic volume decreases. K controls the quasi-incompressibility of the myocardial motion, the higher K the closer to incompressibility the motion. We noticed that incompressibility is an important factor to recover some torsion during the isovolumetric phases.

3.2.3 Heamodynamic Model Parameters

Since the list of parameters that influence the heamodynamic constraint is important, we consider here only the Windkessel parameters, that mainly act on the aortic pressure. The atrial pressure is supposed to be known, this pressure only impacts the fast filling period. We can also vary the initial and the asymptotic aortic pressures, but they only translate the resulting pressure curves. Therefore we use default values from the literature (Schäffler and Schmidt, 1999).

Results are presented in Fig. 8 on the pressure curves only. The peripheral resistance R_p strongly acts on the maximum pressure but also on the length of the isovolumetric relaxation. The characteristic time τ influences the maximum of pressure whereas the characteristic resistance Z_c and the total arteria inertance L change the shape of the pressure during the ejection.

The effects of parameter interactions on the minimum volume V_{min} was also studied. Fig. 9 shows that the proposed sensitivity analysis holds at various operating points. Therefore the performed sensitivity analysis enables to draw conclusions on the selection of the most influential parameters.

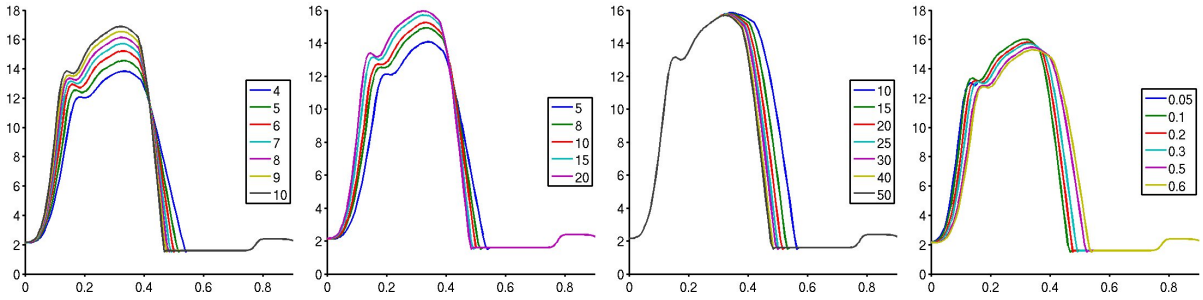

(a) σ_0 (b) k_{ATP} (c) k_{RS} (d) μ

Fig. 6: Pressure evolution (in *kPa*) over time (in *s*) for the left ventricle, with varying active parameters.

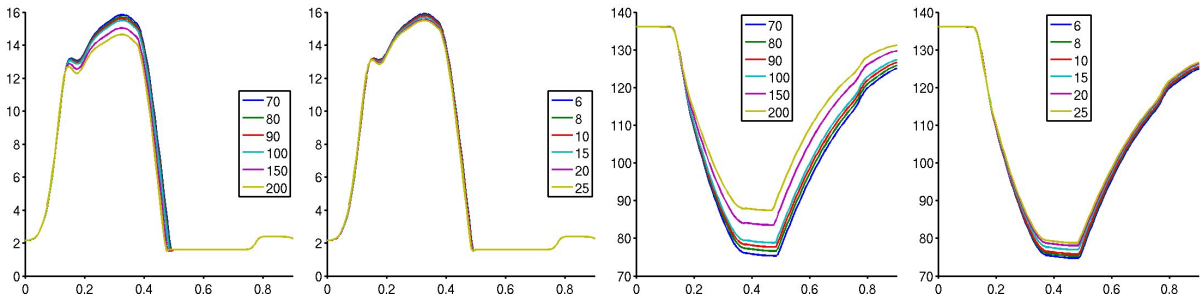

(a) c_1 (b) K (c) c_1 (d) K

Fig. 7: Pressure (in *kPa*) and volume (in *mL*) evolution over time (in *s*) for the left ventricle, with varying passive parameters.

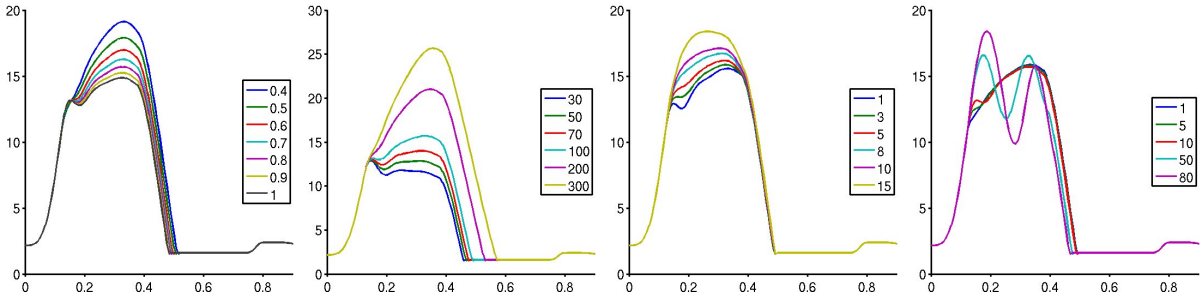

(a) τ (b) R_p (c) Z_c (d) L

Fig. 8: Pressure evolution (in *kPa*) over time (in *s*) for the left ventricle, with varying Windkessel parameters.

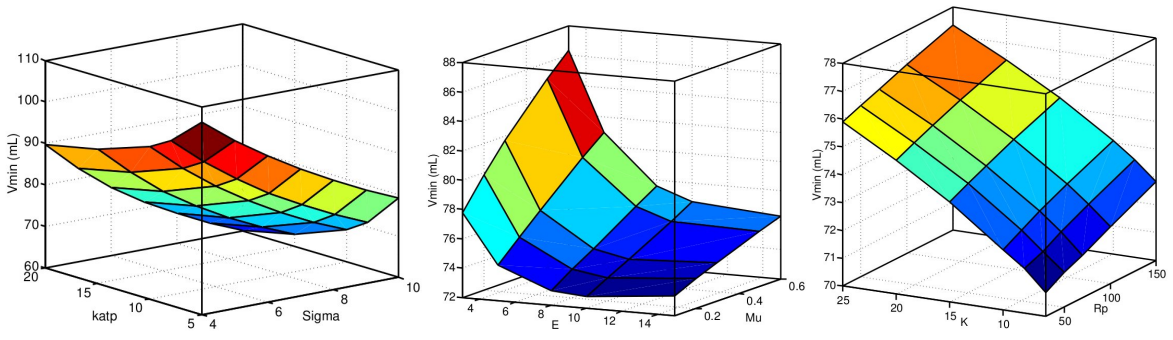

(a) σ_0 and K_{atp} (b) E and μ (c) R_p and K

Fig. 9: Effects of parameter interactions on V_{min}. Varying two parameters in a grid leads to a similar global trend.

3.2.4 Qualitative and Quantitative Justification of the Parameter Selection

Selection from the Sensitivity Analysis

From the curves presented earlier, we fixed k_{atp} because its impact on the observations is coupled with the impact of the maximum contraction σ_0. The same conclusions follow for the passive parameters which all act in the same direction, therefore we only estimated the bulk modulus K. We noticed that the linear modulus E_s and the viscosity parameter μ have similar behaviour, we therefore estimated only μ. We fixed the cross-bridges unfasten rate α and the maximum stiffness k_0 which do not have an impact as strong as the other parameters. Finally the peripheral resistance R_p was also estimated since it acts significantly on the slopes and ejection fraction. Not considering the other valve model parameters since no data is usually available on the pressure, we were left with the following five parameters $(\sigma_0, k_{rs}, \mu, K, R_p)$ to estimate.

Selection from the Singular-Value Decomposition

The Singular-Value Decomposition (SVD) led to left singular vectors representing the eigenvectors of $\mathbf{Cov}(\mathbf{X},\mathbf{Z})\mathbf{Cov}(\mathbf{X},\mathbf{Z})^T$. The first three singular vectors only were considered (since there were only three observations). They depended mainly on the four parameters (σ_0, K, R_p, μ) and slightly on k_{rs}. This analysis led us to try both $\mathbf{X} = \mathbf{X4} = [\sigma_0, \mu, K, R_p]$ and $\mathbf{X} = \mathbf{X5} = [\sigma_0, K, R_p, \mu, k_{rs}]$ for the automatic calibration which is coherent with the previous selection of parameters provided by the sensitivity analysis.

3.3 Calibration Results on Synthetic and Healthy cases

To evaluate the calibration technique, several tests were performed.

3.3.1 Synthetic Data

First, tests on synthetic data were performed to verify the effectiveness of the method. We simulated a cardiac cycle with known parameters and extracted the resulting ventricular volume curve as detailed in B. The application of the calibration method on this synthetic volume curve led to 4 or 5 parameters supposed to produce the same volume curve. Indeed, a good match was found with the volume curve and its derivative as shown in Fig. 10. The mean relative error between the data Z^{obs} and the observations obtained after parameter calibration Z^{new} was less than 1%. No differences were noticeable between the estimation of 4 parameters or 5 parameters.

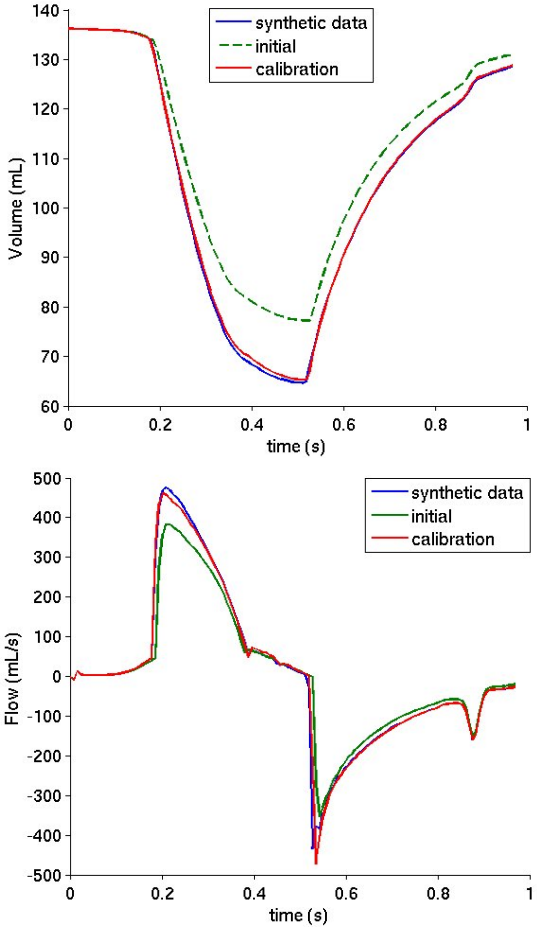

Fig. 10: Results of the calibration technique on synthetic data on the volume evolution in mL(top) and the outward flow function in $mL.s^{-1}$ (bottom).

Therefore, this calibration technique allows to estimate 4 (or 5) influential parameters after performing 9 (or 11) independent simulations (that can be launched in parallel). Hence, this technique is fast and is suitable to be applied on a large database of patients. Table 2 compares the parameters used to simulate the data and the estimated ones. It shows that the solution is not unique due to parameter observability issues and possible correlation between the parameters that lead to the non-uniqueness of the solution for these observations. More observation would be required to constrain the uniqueness of the parameters.

3.3.2 Volunteer Data

The study was performed on seven healthy hearts provided by the STACOM challenge. The electrophys-

Table 2: Parameters values found by the calibration algorithm on synthetic data for 4 parameters.

	σ (MPa)	K (MPa)	R_p (MPa)	μ (MPa.s)
Data	10	10	80	0.2
X4	9.5	12.9	83	0.3

iological model was simulated with standard values of the conductivity and the anisotropic ratio. From the kinematic personalization, we registered all images on the end diastolic image. Then, image transformations were applied to the end-diastolic tetrahedral mesh to estimate the volume of the ventricles over time and then the observation vector $\mathbf{Z}^{obs}$. The calibration required launching 9 (or 11) simulations around the mean parameter vector $\mathbf{X}^0 = [7, 13, 100, 0.28]$ and 4 (or 5) parameters were then estimated based on the Unscented Transform algorithm. Fig. 11 shows the measured, reference and estimated volume curves on case 3.

Fig. 12 shows two views of the estimated cardiac motion overlapped with the MRI sequence at different times of the cycle. The meshes seem to follow reasonably well the images at each phase of the cardiac cycle. Differences may be explained by segmentation errors on the first image, by registration errors or model errors.

Trying to estimate 4 or 5 parameters in all of the cases showed that the results are either similar, or better with 4 parameters than with 5. Therefore only the variation of 4 parameters was studied. A statistical diagram on Fig. 13 gives the median and variance of all cases on values normalized by $\mathbf{X}^0 = [7,\ 13,\ 100,\ 0.28]$. The distribution for healthy cases is rather smooth, R_p has the largest variance of about 12%. These mean values are partially in agreement with what Chabiniok et al (2011) estimated with a similar model. Indeed, our Bulk modulus ($K \sim 10$) is in the range $[1-10]$ they gave, whereas our contractility is higher ($\sigma_0 \sim 5$ instead of $\sigma_0 \sim 0.5$). These differences can be due to the pathology they studied, the differences in the boundary conditions or their local approach to find the parameters which differs from our global technique.

Errors between the real observations $\mathbf{Z}^{obs}$ and the simulated observations $\mathbf{Z}^{new}$ are given in Table 3.

For all cases, the match is excellent for the minimum volume and hence the ejection fraction, but less good ($\simeq 15\%$) for the slopes. In all cases the calibration enables a significant improvement (as shown on Fig.14). Errors can be explained in several ways. First, the real volume curve extracted from the images contains registration errors; then, errors on the geometry,

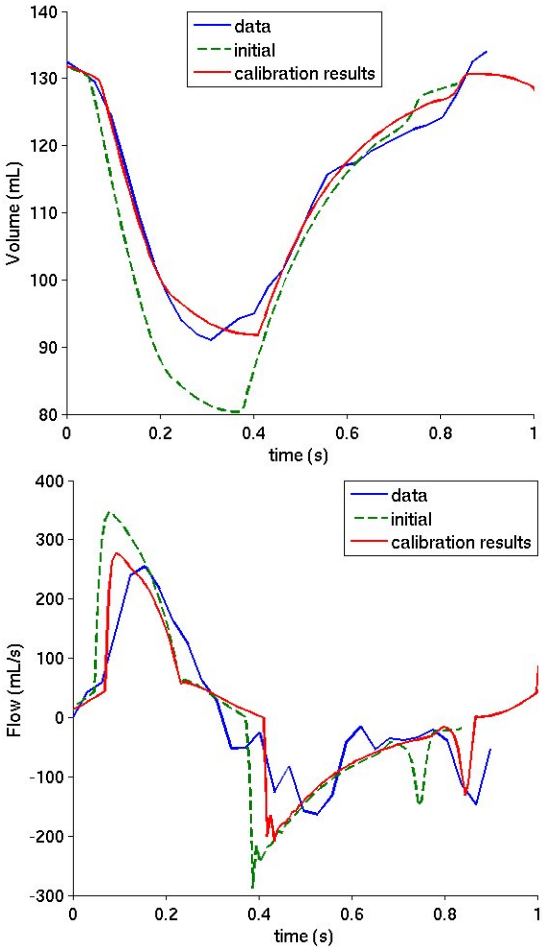

Fig. 11: Results of the calibration technique on real data for one healthy volunteer. (Left) Volume evolution in mL. (Right) Flow evolution in $mL.s^{-1}$.

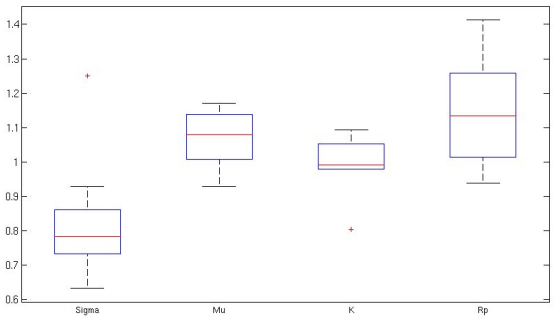

Fig. 13: Box plot showing the median and variance of the parameters for seven healthy cases. The values are normalized by the mean parameter $\mathbf{X}^0$.

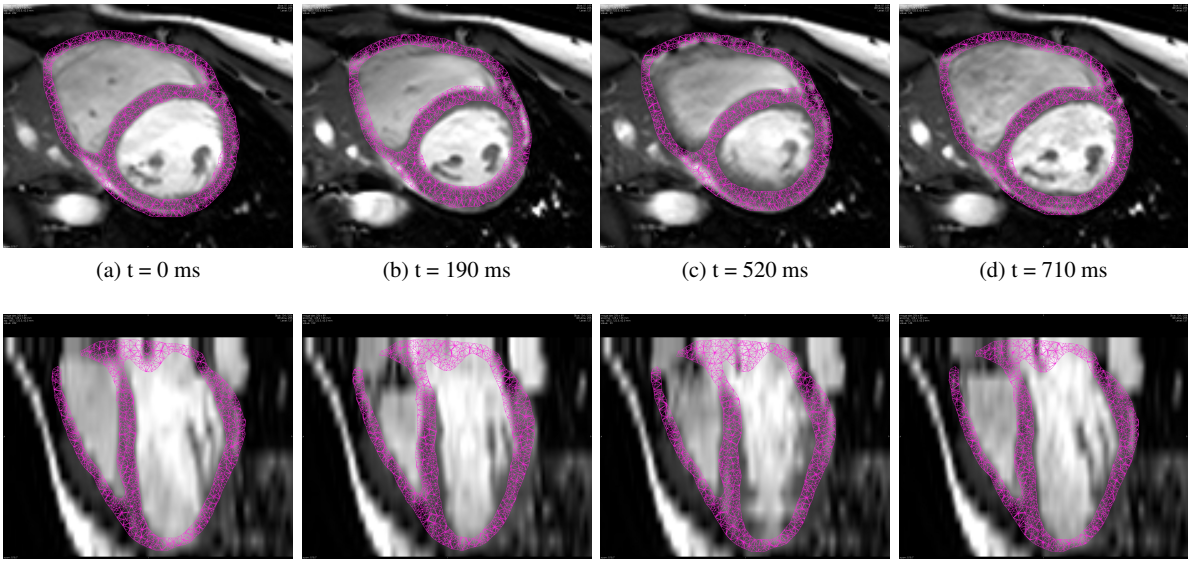

(a) t = 0 ms (b) t = 190 ms (c) t = 520 ms (d) t = 710 ms

(e) t = 0 ms (f) t = 190 ms (g) t = 520 ms (h) t = 710 ms

Fig. 12: Short axis and long axis views of the simulated mesh on top of the MR images at different moments of the cardiac cycle (heart period = 930 ms) for case 3.

Table 3: Relative errors (in %) between simulated results $\mathbf{Z}^{new}$ and real data $\mathbf{Z}^{obs}$ on the 7 healthy cases

Volunteers	1	2	3	4	5	6	7	Mean	Min	Max
V_{min}	0.35	3.51	0.83	0.79	1.09	1.38	1.31	1.26	0.35	3.51
q_{max}	3.06	20.99	8.57	21.37	11.5	12.1	5.36	14.29	3.06	21.37
q_{min}	0.31	4.12	27.41	6.48	27.58	16.92	5.81	15.18	0.31	27.58

the fibers and electrophysiology add to these results. Finally, the choice of the calibrated parameters is not unique and influences the results.

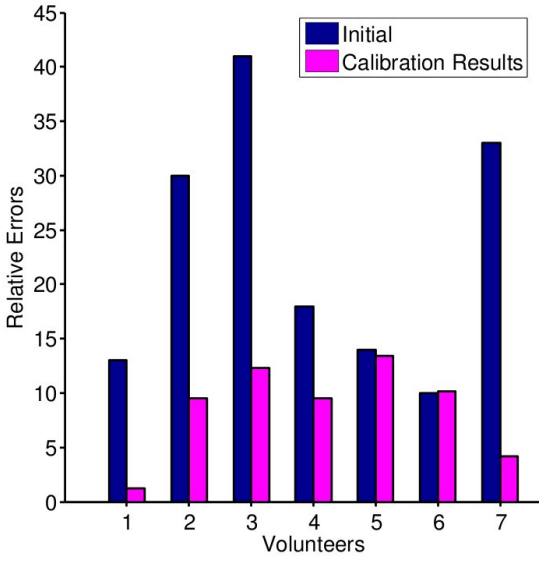

Fig. 14: Relative errors (in %) on the observations before and after calibration.

3.3.3 Evaluation of Registration Error Influence

We tried to evaluate the error in the registration technique to understand whether the model could actually match the data better than shown on Fig. 11. For this purpose, we created synthetic images (as done by (Prakosa et al, 2011)) from a real sequence, using the deformed meshes resulting from a simulation. This technique creates new cardiac cine-MRI sequences combining the deformation field computed by the simulation and the deformation field computed by the image registration of the real sequence. We then registered this new sequence with the iLogDemons algorithm, and extracted the volume curves from the resulting registered meshes. We expect to have similar curves since images are created from the same electromechanical model of the heart. The comparison between the initial simulated volume curve and the one computed after registration is given in Fig. 15. The relative error is about 25% for both slopes and 3% for V_{min}. These errors indicate that the model may not be able to better match these registered volume curves. This can be due to registration errors as well as modelling errors.

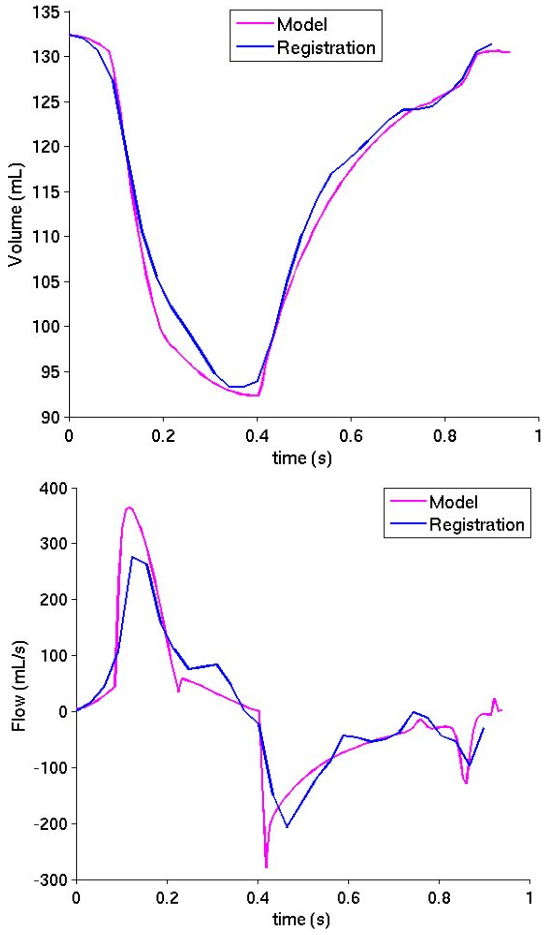

Fig. 15: Comparison between the volume variation computed from the simulation and the one estimated from registered images (in mL).

4 Discussion and Conclusion

In this paper we proposed an innovative calibration method of an electromechanical cardiac model. The complete model depends on 16 parameters that act on the active, passive and constraint components. The calibration based on Unscented Transform allowed us to give a fast initialization of 4 or 5 parameters, leaving the other 12 or 11 fixed to standard values. The choice of these 4 (or 5) parameters was made based on a sensitivity analysis on the volume variation and were confirmed by Singular-Value Decomposition analysis. Since the calibration requires only to run several simulations in parallel to estimate these parameters followed by one additional simulated cycle to verify the results, it can easily be used as a preprocessing step before the application of more sophisticated personalization algorithms.

The creation of a synthetic image sequence allowed us to measure the intrinsic error in estimating volume curves over time. Since this error is of the same order of magnitude as the one after model calibration on healthy cases, we can conclude that the calibration enables the best possible match of the volume curve given the registration and the modelling errors, on 7 healthy volunteers. Furthermore, the calibration provided consistent and plausible range of values for the parameters.

This work could be extended in several ways. For instance, fibre orientations which is important to model electrical and mechanical behaviours may be based on a registered human atlas built from DT-MRI (Lombaert et al, 2011) or from *in-vivo* patient specific imaging (Toussaint et al, 2010). Furthermore, the parameters of the registration algorithm could be optimized to better track the cardiac motion. An alternative for image registration is to use a physically based model (Wong et al, 2010) which may include more *a priori* knowledge about the cardiac motion.

Another extension of this work would be to include more observations such as global indices of the cardiac motion or endocardial pressures (if available). Indeed, volume curves provide basic information about the cardiac cycle and ejection fraction. A larger set of parameters could be estimated by adding global or even regional motion indices such as radial, longitudinal or circumferential displacements or strains in the ventricles or AHA segments.

To conclude, we proposed an efficient calibration method to quickly assess the main parameters of a cardiac model. The authors believe that this calibration can replace manual personalization based on trial and error, before the application of advanced automatic personalization algorithms from medical images.

Acknowledgements This work is partially funded by the European project *euHeart* (http://www.euheart.eu) FP7-2007-2013-224495 and by the ERC advanced Grant MedYMA. The authors warmly thank Kristin McLeod, Adityo Prakosa, Loïc Le Folgoc, Ján Margeta and Jatin Relan from Asclepios team for their support and constructive discussions, as well as Radomir Chabiniok, Dominique Chapelle and Michel Sorine, for their expertise on the model.

A Active Force Calculation

To solve the coupled equations (2), we reformulate into

$$\dot{\mathbf{X}} = \begin{pmatrix} -r & \dot{ec} \\ 0 & -r \end{pmatrix} \mathbf{X} + n_0 \mid u \mid_+ \begin{pmatrix} \sigma_0 \\ k_0 \end{pmatrix}$$

where $\mathbf{X} = (\tau_c, k_c)$, $r = (\mid u \mid + \alpha \mid \dot{e_c} \mid)$. This is solved using Euler Implicit Solver for instance, and it gives at each time step the couple (τ_c^n, k_c^n).

The contraction stress at each time step $\sigma_c^n = E_s(e_{1D}^n - e_c^n)$ is given easily once we have e_c^n. Since $\sigma_c = E_s(e_{1D} - e_c) = \tau_c +$

$\mu \dot{e_c}$, we obtain a recursive equation for e_c^n:

$$e_c^{n+1} = \frac{\Delta t E_s}{\mu} e_{1D}^n + \left(1 - \frac{\Delta t E_s}{\mu}\right) e_c^n - \frac{\Delta t}{\mu} \tau_c^n$$

where τ_c^n is given by solving the coupled equations. Therefore we determine the applied force and stiffness using the Total Lagrangian approach with Finite Elements Methods (Delingette and Ayache, 2004). The contraction force $\mathbf{F}_i$ on each deformed vertex $\mathbf{Q}_i$ and the stiffness matrix $\mathbf{K}_{ij}$ on each edge are given by:

$$\mathbf{F}_i = -\frac{1}{4} \nabla\phi \sigma_c (\mathbf{f} \otimes \mathbf{f}) \mathbf{D}_i$$

and

$$\mathbf{K}_{ij} = \frac{\sigma_c}{4} \mathbf{Id} (\mathbf{D}_j^T \mathbf{f} \otimes \mathbf{f} \mathbf{D}_i) + \frac{\partial \sigma_c}{\partial \mathbf{Q}_j} \mathbf{D}_i^T \mathbf{f} \otimes \mathbf{f} \nabla\phi^T$$

where $\mathbf{f}$ is the fibre direction and $\mathbf{D}_i$ is a shape vector at initial vertex $\mathbf{P}_i$.

We need to differentiate the contraction stress with respect to the nodal point. We start with the definition of the contraction stress $\sigma_c = E_s(e_{1D} - e_c)$ and $e_{1D} = \mathbf{f}^T \mathbf{E} \mathbf{f}$. The Green-Lagrange deformation tensor can be written

$$\mathbf{E} = -\frac{1}{4} \sum_k \sum_{l \neq k} (\|\mathbf{Q}_k - \mathbf{Q}_l\|^2 - \|\mathbf{P}_k - \mathbf{P}_l\|^2)(\mathbf{D}_k \otimes \mathbf{D}_l + \mathbf{D}_l \otimes \mathbf{D}_k)$$

$$e_{1D} = -\frac{1}{2} \sum_{l \neq k} \|\mathbf{Q}_k - \mathbf{Q}_l\|^2 (\mathbf{f}^T \mathbf{D}_k \mathbf{D}_l^T \mathbf{f}) + \|\mathbf{P}_k - \mathbf{P}_l\|^2 (\mathbf{f}^T \mathbf{D}_k \mathbf{D}_l^T \mathbf{f})$$

$$\frac{\partial e_{1D}}{\partial \mathbf{Q}_j} = -\sum_{i \neq j} (\mathbf{Q}_j - \mathbf{Q}_i) \mathbf{D}_i^T \mathbf{f} \mathbf{D}_j^T \mathbf{f}$$

Using the definitions of the deformation gradient $\nabla\phi = \sum_i \mathbf{Q}_i \mathbf{D}_i^T$ and the fact that $\sum_{i=1}^4 \mathbf{D}_i = 0$, we rewrite the last equation into:

$$\frac{\partial e_{1D}}{\partial \mathbf{Q}_j} = \mathbf{Q}_j (-\sum_{i \neq j} \mathbf{D}_i^T) \mathbf{f} \mathbf{D}_j^T \mathbf{f} + (\sum_{i \neq j} \mathbf{Q}_i \mathbf{D}_i^T) \mathbf{f} \mathbf{D}_j^T \mathbf{f} = \nabla\phi \mathbf{f} \mathbf{D}_j^T \mathbf{f}$$

Therefore

$$\frac{\partial \sigma_c}{\partial \mathbf{Q}_j} = E_s \nabla\phi \mathbf{f} \mathbf{D}_j^T \mathbf{f}$$

B Heamodynamic Model

B.1 Relation between nodal displacements and ventricular volumes

We compute the volume of the ventricle (open surface mesh Z) as a sum of the tetrahedra that are formed by each triangle on the surface and a unique point, for instance the point $\mathbf{O}$. Let $\mathbf{Q}_k$ be the deformed points on the surface with each unit volume of tetrahedron T_i given by $V_i = \frac{1}{6} |\mathbf{Q}_{T_i(0)}, \mathbf{Q}_{T_i(1)}, \mathbf{Q}_{T_i(2)}|$, where $|.,.,.|$ is the mix product. If the surface is closed, the total volume is the sum of the unit volumes over all the triangles.

For an open surface mesh, with N holes, we virtually close each of the holes n by a point $\mathbf{C}_n$ - the barycenter of the N_n points on the border named $\mathbf{Q}_{H_n(k)}$:

$$\mathbf{C}_n = \frac{1}{N_n} \sum_{k=0}^{N_n - 1} \mathbf{Q}_{H_n(k)}$$

Therefore the total volume of the ventricle can be written as:

$$V_{total} = \sum_{T_i \in Z} V_i + \sum_n \sum_{k=0}^{N_n - 1} \frac{1}{6} |\mathbf{Q}_{H_n(k)}, \mathbf{Q}_{H_n(k+1)}, \mathbf{C}_n| \tag{9}$$

B.2 Derivatives of the volume

We obtain the vector $\mathbf{G}_L$ (respectively $\mathbf{G}_R$), by differentiating the volume with respect to the nodal positions on the surface.

– *Inside Points*:

Let's define the area vector of a triangle T_i:

$$\mathbf{A}(T_i) = \frac{\mathbf{Q}_{T_i(0)} \times \mathbf{Q}_{T_i(1)} + \mathbf{Q}_{T_i(1)} \times \mathbf{Q}_{T_i(2)} + \mathbf{Q}_{T_i(2)} \times \mathbf{Q}_{T_i(0)}}{2}$$

then we need to sum over all the triangles that surround the point $\mathbf{Q}_i$.

$$\frac{\partial V}{\partial \mathbf{Q}_i} = \frac{1}{3} \sum_{T_j \supset \mathbf{Q}_i} \mathbf{A}(T_j)$$

– *Border Points*:

To this derivative, the contribution of $\frac{1}{6} |\mathbf{Q}_{H_j(k)}, \mathbf{Q}_{H_j(k+1)}, \mathbf{C}_j|$ has to be added. It gives therefore

$$\begin{aligned} \frac{\partial V}{\partial \mathbf{Q}_{H_n(i)}} =& \frac{1}{3} \sum_{T_j \supset \mathbf{Q}_{H_n(i)}} \mathbf{A}(T_j) \\ &+ \frac{\mathbf{Q}_{H_n(i)} \times \mathbf{Q}_{H_n(i+1)}}{6} + \frac{\mathbf{Q}_{H_n(i+1)} \times \mathbf{C}_n}{6} \\ &+ \frac{\mathbf{C}_n \times \mathbf{Q}_{H_n(i-1)}}{6} + \frac{\mathbf{Q}_{H_n(i-1)} \times \mathbf{Q}_{H_n(i)}}{6} \end{aligned} \tag{10}$$

– *Second Derivative for inside points*:

We want to differentiate $\frac{\partial V}{\partial \mathbf{Q}_i}$ with respect to $\partial \mathbf{Q}_k$. When we sum the area vectors over all the triangles that surround ∂Q_i, many terms are cancelled, and many do not include ∂Q_k. For the derivative, only two terms remain:

$$\frac{\partial^2 V}{\partial \mathbf{Q}_k \partial \mathbf{Q}_i} = \frac{1}{6} \frac{\partial}{\partial \mathbf{Q}_k} (\mathbf{Q}_k \times \mathbf{Q}_v + \mathbf{Q}_u \times \mathbf{Q}_k)$$

where $(\mathbf{Q}_k, \mathbf{Q}_v, \mathbf{Q}_i)$ and $(\mathbf{Q}_u, \mathbf{Q}_k, \mathbf{Q}_i)$ are two oriented triangles. The second derivative is then:

$$\frac{\partial^2 V}{\partial \mathbf{Q}_k \partial \mathbf{Q}_i} = \frac{1}{6} \begin{pmatrix} 0 & -b_3 & b_2 \\ b_2 & 0 & -b_1 \\ -b_2 & b_1 & 0 \end{pmatrix} \tag{11}$$

where $\mathbf{b} = (b_1, b_2, b_3) = \mathbf{Q}_u - \mathbf{Q}_v$.

– *Second Derivative for border points*:

When $\mathbf{Q}_i$ and $\mathbf{Q}_k$ are on the border, for instance $\mathbf{Q}_i = \mathbf{Q}_{H_n(i)}$ and $\mathbf{Q}_k = \mathbf{Q}_{H_n(i+1)}$, we have to add a vector $\tilde{\mathbf{b}} = \mathbf{Q}_{H_n(i)} - \mathbf{C}_n$ to $\mathbf{b}$.

B.3 Constraint Formulation

In order to model the constraint explained by equation (4), we need to rewrite it in the form of equation (5) for each ventricle. Knowing that $q = -\frac{\Delta V}{\Delta t}$ and $\frac{\Delta V}{\Delta t} = \mathbf{G}^T (\Delta \mathbf{s}^{t+\Delta t} + \mathbf{s}^t)$. For each phase:

– *Filling Phase*:

$q = K_{at}(P_v - P_{at})$ gives

$$\begin{cases} D = K_{at} \\ F_D = K_{at} P_{at}^{t+\Delta t} - \mathbf{G}^T \mathbf{s}^t \end{cases}$$

– *Isovolumetric Phases*:

$q = K_{iso}(P_v - P_{at})$ gives

$$\begin{cases} D = K_{iso} \\ F_D = K_{iso} P_{at}^{t+\Delta t} - \mathbf{G}^T \mathbf{s}^t \end{cases}$$

For those two phases we need to know $P_{at}^{t+\Delta t}$ which is modelled as two sigmoids following Billet's description (Billet, 2010).

– *Ejection Phase*:

$q = K_{ar}(P_v - P_{ar}) + K_{iso}(P_{ar} - P_{at})$. We need to estimate $P_{ar}^{t+\Delta t}$. To this end, we can use several Windkessel models (two, three, or four elements). The method to derive the constraint equation is the same for each of them, hence we only describe here the technique for the four-element Windkessel model which is the most accurate but complex one. The four-element Windkessel equation relates the pressure of the aorta P_{ar} (or pulmonary vein) to the flow and its first two derivatives:

$$R_p C \dot{P_{ar}} + P_{ar} - P_{ve} = (R_p + Z_c)q + (R_p Z_c C + L)\dot{q} + L R_p C \ddot{q} \quad (12)$$

with P_{ve} the venous pressure, R_p the peripheral resistance, C the total arterial compliance, Z_c the characteristic impedance, and L the total arterial inertance ($L = 0$ reduces the equation to the three-element Windkessel). We denote $\tau = R_p C$ the characteristic time. We use Euler Implicit integration scheme, therefore

$$\dot{q} = \frac{q^{t+\Delta t} - q^t}{\Delta t} \ , \dot{P_{ar}} = \frac{P_{ar}^{t+\Delta t} - P_{ar}^t}{\Delta t}$$

$$\text{and } \ddot{q} = \frac{1}{\Delta t}\left(\frac{q^{t+\Delta t} - q^t}{\Delta t} - \dot{q}^t\right)$$

From $q = K_{ar}(P_v - P_{ar}) + K_{iso}(P_{ar} - P_{at})$ we extract

$$P_{ar}^{t+\Delta t} = \frac{q^{t+\Delta t} - K_{ar} P_v^{t+\Delta t} + K_{iso} P_{at}^{t+\Delta t}}{K_{iso} - K_{ar}}$$

that we inject into equation (12). We thus obtain:

$$\begin{cases} d_0 = \left(\frac{\tau}{\Delta t} + 1\right)\left(\frac{1}{K_{ar} - K_{iso}} + Z_c\right) + R_p + \frac{L}{\Delta t} + \frac{L\tau}{\Delta t^2} \\ d_1 = \frac{K_{ar}}{K_{ar} - K_{iso}}\left(\frac{\tau}{\Delta t} + 1\right) \\ P = \frac{\tau}{\Delta t} P_{ar}^t + P_{ve} + \frac{K_{iso}}{K_{ar} - K_{iso}}\left(\frac{\tau}{\Delta t} + 1\right) P_{at}^{t+\Delta t} \\ \quad - \left(\frac{\tau Z_c + L}{\Delta t} - \frac{L\tau}{\Delta t^2}\right) q^t - \frac{L\tau}{\Delta t}\dot{q}^t \\ D = d_1 / d_0 \\ F_D = P/d_0 - \mathbf{G}^T \mathbf{s}^t \end{cases}$$

References

Bestel J, Clement F, Sorine M (2001) A biomechanical model of muscle contraction. Medical Image Computing and Computer Assisted Intervention (MICCAI) pp 1159–1161

Billet F (2010) Assimilation de données images pour la personnalisation d'un modèle électromécanique du coeur. PhD thesis, Université de Nice -Sophia Antipolis, in French

Chabiniok R (2011) Personalized biomechanical heart modeling for clinical applications. PhD thesis, Université Pierre et Marie Curie - Paris 6

Chabiniok R, Moireau P, Lesault P, Rahmouni A, Deux J, Chapelle D (2011) Estimation of tissue contractility from cardiac cine-MRI using a biomechanical heart model. Biomechanics and Modeling in Mechanobiology pp 1–22

Chapelle D, Le Tallec P, Moireau P, Sorine M (2012) An energy-preserving muscle tissue model: formulation and compatible discretizations. International Journal for Multiscale Computational Engineering 10(2):189–211

Costa KD, Holmes J, McCulloch AD (2001) Modelling cardiac mechanical properties in three dimensions. Phil Trans R Soc Lond 359:1233–1250

Delingette H, Ayache N (2004) Soft Tissue Modeling for Surgery Simulation. In: Computational Models for the Human Body, Elsevier, pp 453–550

Delingette H, Billet F, Wong KCL, Sermesant M, Rhode K, Ginks M, Rinaldi CA, Razavi R, Ayache N (2011) Personalization of Cardiac Motion and Contractility from Images using Variational Data Assimilation. IEEE transactions on biomedical engineering In Press

Ecabert O, Peters J, Walker MJ, Ivanc T, Lorenz C, von Berg J, jonathan Lessick, mani Vembar, Weese J (2011) Segmentation of the heart and great vessels in CT images using a model-based adaptation framework. Medical Image Analysis 15(6):863–876

Holzapfel G, Ogden R (2009) Constitutive modelling of passive myocardium: a structurally based framework for material characterization. Philosophical Transactions of the Royal Society A: Mathematical, Physical and Engineering Sciences 367(1902):3445–3475

Humphrey J, Strumpf R, Yin F (1990) Determination of a constitutive relation for passive myocardium: I. a new functional form. Journal of biomechanical engineering 112:333

Hunter P, Nash M, Sands G (1997) Computational electromechanics of the heart. Computational biology of the heart pp 345–407

Huxley A (1957) Muscle structure and theories of contraction. Progress in biophysics and biophysical chemistry 7:255

Julier S, Uhlmann J (1997) A new extension of the Kalman filter to nonlinear systems. In: Int. Symp. Aerospace/Defense Sensing, Simul. and Controls, Citeseer, vol 3, p 26

Kerckhoffs RCP (ed) (2010) Patient-Specific Modeling of the Cardiovascular System, Technology-Driven Personalized Medicine. Springer

Larrabide I, Omedas P, Martelli Y, Planes X, Nieber M, Moya J, Butakoff C, Sebastián R, Camara O, De Craene M, et al (2009) Gimias: an open source framework for efficient development of research tools and clinical prototypes. Functional Imaging and Modeling of the Heart pp 417–426

Liu H, Shi P (2009) Maximum a posteriori strategy for the simultaneous motion and material property estimation of the heart. Biomedical Engineering, IEEE Transactions on 56(2):378–389

Lombaert H, Peyrat JM, Croisille P, Rapacchi S, Fanton L, Clarysse P, Delingette H, Ayache N (2011) Statistical Analysis of the Human Cardiac Fiber Architecture from DT-MRI. In: Axel L, Metaxas D (eds) Proceedings of FIMH Conference 2011, Springer, LNCS, vol 6666, pp 171–179, best Paper Award

Mansi T, Pennec X, Sermesant M, Delingette H, Ayache N (2011) iLogDemons: A demons-based registration algorithm for tracking incompressible elastic biological tissues. International Journal of Computer Vision 92(1):92–111

Marchesseau S, Heimann T, Chatelin S, Willinger R, Delingette H (2010) Fast porous visco-hyperelastic soft tissue model for surgery simulation: application to liver surgery. Progress in Biophysics and Molecular Biology 103(2-3):185–196, DOI 10.1016/j.pbiomolbio.2010.09.005

Mazhari R, McCulloch AD (2000) Effect of laminar orthotropic myofiber architecture on regional stress and strain in the canine left ventricule. Journal of Elasticity 61(4):143–164, DOI 10.1067/mnc.2001.117113

McLeod K, Prakosa A, Mansi T, Sermesant M, Pennec X (2012) An Incompressible Log-Domain Demons Algorithm for Tracking Heart Tissue. In: Proc. MICCAI Workshop on Statistical Atlases and Computational Models of the Heart: Mapping Structure and Function (STACOM11), Springer, Toronto, LNCS, vol 7085, pp 54–65, in press

Moireau P, Chapelle D (2011) Reduced-order Unscented Kalman Filtering with application to parameter identification in large-dimensional systems. COCV 17:380–405, doi:10.1051/cocv/2010006

Nash M (1998) Mechanics and material properties of the heart using an anatomically accurate mathematical model. PhD thesis, University of Auckland

Peyrat JM, Sermesant M, Pennec X, Delingette H, Xu C, McVeigh ER, Ayache N (2007) A Computational Framework for the Statistical Analysis of Cardiac Diffusion Tensors: Application to a Small Database of Canine Hearts. IEEE Transactions on Medical Imaging 26(11):1500–1514, DOI 10.1109/TMI.2007.907286, pMID: 18041265

Prakosa A, Sermesant M, Delingette H, Saloux E, Allain P, Cathier P, Etyngier P, Villain N, Ayache N (2011) Synthetic Echocardiographic Image Sequences for Cardiac Inverse Electro-Kinematic Learning. In: Proceedings of Medical Image Computing and Computer Assisted Intervention (MICCAI), Springer, Heidelberg, Toronto, Canada, LNCS, p 8p

Relan J, Chinchapatnam P, Sermesant M, Rhode K, Ginks M, Delingette H, Rinaldi CA, Razavi R, Ayache N (2011) Coupled Personalization of Cardiac Electrophysiology Models for Prediction of Ischaemic Ventricular Tachycardia. Journal of the Royal Society Interface Focus 1(3):396–407

Sachse F (2004) Computational cardiology: modeling of anatomy, electrophysiology, and mechanics, vol 2966. Springer Verlag

Sainte-Marie J, Chapelle D, Cimrman R, Sorine M (2006) Modeling and estimation of the cardiac electromechanical activity. Computers & structures 84(28):1743–1759

Schäffler A, Schmidt S (1999) Anatomie Physiologie Biologie. In French

Sermesant M, Delingette H, Ayache N (2006) An Electromechanical Model of the Heart for Image Analysis and Simulation. IEEE Transactions in Medical Imaging 25(5):612–625

Sermesant M, Konukoglu E, Delingette H, Coudiere Y, Chinchaptanam P, Rhode K, Razavi R, Ayache N (2007) An anisotropic multi-front fast marching method for real-time simulation of cardiac electrophysiology. In: Proceedings of Functional Imaging and Modeling of the Heart 2007 (FIMH'07), LNCS, vol 4466, pp 160–169

Sermesant M, Chabiniok R, Chinchapatnam P, Mansi T, Billet F, Moireau P, Peyrat J, Wong K, Relan J, Rhode K, Ginks M, Lambiase P, Delingette H, Sorine M, Rinaldi C, Chapelle D, Razavi R, Ayache N (2012) Patient-specific electromechanical models of the heart for the prediction of pacing acute effects in CRT: A preliminary clinical validation. Medical Image Analysis pp 201–215

Smith N, de Vecchi A, McCormick M, Nordsletten D, Camara O, Frangi A, Delingette H, Sermesant M, Relan J, Ayache N, Krueger MW, Schulze W, Hose R, Valverde I, Beerbaum P, Staicu C, Siebes M, Spaan J, Hunter P, Weese J, Lehmann H, Chapelle D, Razavi R (2011) euheart: Personalized and integrated cardiac care using patient-specific cardiovascular modelling. Journal of the Royal Society Interface Focus 1(3):349–364

Sundar H, Davatzikos C, Biros G (2009) Biomechanically-constrained 4D estimation of myocardial motion. Medical Image Computing and Computer-Assisted Intervention–MICCAI 2009 pp 257–265

Tobon-Gomez C, De Craene M, Dahl A, Kapetanakis S, Carr-White G, Lutz A, Rasche V, Etyngier P, Kozerke S, Schaffeter T, Riccobene C, Martelli Y, Camara O, Frangi A, Rhode KS (2011) A multimodal database for the 1st cardiac motion analysis challenge. In: Proc. MICCAI Workshop on Statistical Atlases and Computational Models of the Heart: Mapping Structure and Function (STACOM11), Springer, Toronto, LNCS, vol 7085, pp 32–43, in press

Toussaint N, Stoeck CT, Kozerke S, Sermesant M, Batchelor PG (2010) In-vivo Human 3D Cardiac Fibre Architecture: Reconstruction Using Curvilinear Interpolation of Diffusion Tensor Images. In: Proc. Medical Image Computing and Computer Assisted Intervention (MICCAI'10), Springer, Beijing, China, LNCS, vol 13, pp 418–425

Wan E, Van Der Merwe R (2000) The unscented Kalman filter for nonlinear estimation. In: Adaptive Systems for Signal Processing, Communications, and Control Symposium 2000. AS-SPCC. The IEEE 2000, IEEE, pp 153–158

Wang V, Lam H, Ennis D, Cowan B, Young A, Nash M (2009) Modelling passive diastolic mechanics with quantitative MRI of cardiac structure and function. Medical Image Analysis 13(5):773–784

Wong KC, Wang L, Zhang H, Liu H, Shi P (2008) Simulation of Active Cardiac Dynamics with Orthotropic Hyperelastic Material Model. The MIDAS Journal - Computational Biomechanics for Medicine

Wong KCL, Billet F, Mansi T, Chabiniok R, Sermesant M, Delingette H, Ayache N (2010) Cardiac motion estimation using a proactive deformable model: evaluation and sensitivity analysis. In: MICCAI Workshop on Statistical Atlases and Computational Models of the Heart: Mapping Structure and Function (STACOM) and a Cardiac Electrophysiological Simulation Challenge (CESC'10), Springer, LNCS, vol 6364, pp 154–163

Xi J, Lamata P, Lee J, Moireau P, Chapelle D, Smith N (2011) Myocardial transversely isotropic material parameter estimation from in-silico measurements based on a reduced-order unscented Kalman filter. Journal of the Mechanical Behavior of Biomedical Materials